PLOS ONE

RESEARCH ARTICLE

Water-Exchange-Modified Kinetic Parameters from Dynamic Contrast-Enhanced MRI as Prognostic Biomarkers of Survival in Advanced Hepatocellular Carcinoma Treated with Antiangiogenic Monotherapy

Sang Ho Lee[1], Koichi Hayano[2], Andrew X. Zhu[3], Dushyant V. Sahani[2], Hiroyuki Yoshida[1]*

1 3D Imaging Research, Department of Radiology, Massachusetts General Hospital and Harvard Medical School, Boston, Massachusetts, United States of America, **2** Division of Abdominal Imaging and Intervention, Department of Radiology, Massachusetts General Hospital, Boston, Massachusetts, United States of America, **3** Massachusetts General Hospital Cancer Center, Boston, Massachusetts, United States of America

* yoshida.hiro@mgh.harvard.edu

OPEN ACCESS

Citation: Lee SH, Hayano K, Zhu AX, Sahani DV, Yoshida H (2015) Water-Exchange-Modified Kinetic Parameters from Dynamic Contrast-Enhanced MRI as Prognostic Biomarkers of Survival in Advanced Hepatocellular Carcinoma Treated with Antiangiogenic Monotherapy. PLoS ONE 10(9): e0136725. doi:10.1371/journal.pone.0136725

Editor: Sheng-Nan Lu, Kaohsiung Chang Gung Memorial Hospital, TAIWAN

Received: May 27, 2015

Accepted: August 8, 2015

Published: September 14, 2015

Data Availability Statement: All relevant data are within the paper and its Supporting Information files.

Funding: Part of this work was supported by the National Institutes of Health grant (http://grants.nih.gov/grants/oer.htm) of R21CA187877 (PI: Yoshida). National Institutes of Health had a role in supporting, through the above grant, the development of the software that implemented kinetic models used for the analysis of the DCE-MRI data in this study. The majority of the study presented in manuscript was done under the "work made for hire" by the affiliated

Abstract

Background

To find prognostic biomarkers in pretreatment dynamic contrast-enhanced MRI (DCE-MRI) water-exchange-modified (WX) kinetic parameters for advanced hepatocellular carcinoma (HCC) treated with antiangiogenic monotherapy.

Methods

Twenty patients with advanced HCC underwent DCE-MRI and were subsequently treated with sunitinib. Pretreatment DCE-MRI data on advanced HCC were analyzed using five different WX kinetic models: the Tofts-Kety (WX-TK), extended TK (WX-ETK), two compartment exchange, adiabatic approximation to tissue homogeneity (WX-AATH), and distributed parameter (WX-DP) models. The total hepatic blood flow, arterial flow fraction (γ), arterial blood flow (BF_A), portal blood flow, blood volume, mean transit time, permeability-surface area product, fractional interstitial volume (v_I), extraction fraction, mean intracellular water molecule lifetime (τ_C), and fractional intracellular volume (v_C) were calculated. After receiver operating characteristic analysis with leave-one-out cross-validation, individual parameters for each model were assessed in terms of 1-year-survival (1YS) discrimination using Kaplan-Meier analysis, and association with overall survival (OS) using univariate Cox regression analysis with permutation testing.

Results

The WX-TK-model-derived γ ($P = 0.022$) and v_I ($P = 0.010$), and WX-ETK-model-derived τ_C ($P = 0.023$) and v_C ($P = 0.042$) were statistically significant prognostic biomarkers for 1YS.

institution (MGH), which is, by nature, not an explicit funding dedicated to the study. Thus, there is no explicit funding other than what was stated.

Competing Interests: The authors have declared that no competing interests exist.

Increase in the WX-DP-model-derived BF_A ($P = 0.025$) and decrease in the WX-TK, WX-ETK, WX-AATH, and WX-DP-model-derived v_C ($P = 0.034$, $P = 0.038$, $P = 0.028$, $P = 0.041$, respectively) were significantly associated with an increase in OS.

Conclusions

The WX-ETK-model-derived v_C was an effective prognostic biomarker for advanced HCC treated with sunitinib.

Introduction

Dynamic contrast-enhanced MRI (DCE-MRI) has a potential role in the monitoring of antiangiogenic therapy for hepatocellular carcinoma (HCC) [1–3]. Pharmacokinetic analysis of DCE-MRI data is widely applied in oncology for the measurement of vascular and tissue physiology. Extracted kinetic parameters are used for the characterization and classification of disease processes and for monitoring of treatment effects. The reliability of these measurements depends on the use of a model that accurately describes the relationship of the contrast agent (CA) concentration to the underlying tissue physiology. Because the liver receives a dual blood supply from the hepatic artery and the portal vein, dual-input tracer kinetic models hold promise for quantitative analysis of hepatic perfusion [4–7].

However, it is still unclear to what extent modeling assumptions, particularly regarding water exchange between tissue compartments, impact on parameter estimates derived from DCE-MRI data. The commonly used standard approach to DCE-MRI data analysis does not take water exchange into account, thus effectively assuming that water exchange is at the fast exchange limit (FXL) [8]. However, this assumption is physically unreasonable because deviations from the FXL condition occur when the compartmental distributions of CA and water molecules are different [9–11]. Water-exchange-modified (WX) tracer kinetic analysis of DCE-MRI data allows evaluation of intercompartmental water interchange kinetics, thus enabling additional estimation of the rate of cellular water turnover, which may play a role as a surrogate marker for quantifying the most crucial ongoing cellular metabolic turnover [12]. Therefore, it is warranted to use a model that includes water exchange effects in order to demonstrate whether water exchange has an impact on the prediction of the clinical outcome.

To date, no effort has been made to seek data comparing the relative performance of different tracer kinetic models that measure intercompartmental water exchange kinetics in DCE-MRI data regarding HCC. Our aim in this study was to find effective prognostic kinetic biomarkers of advanced HCC treated with sunitinib monotherapy for 1-year survival (1YS) and overall survival (OS), in comparison with five different WX dual-input tracer kinetic models for pretreatment liver DCE-MRI.

Materials and Methods

Subjects

The protocol for this phase II clinical trial on advanced HCC [1] was in compliance with Health Insurance Portability and Accountability Act regulations and was approved by the institutional review board at Dana-Farber/Harvard Cancer Center (Boston, MA). All patients were required to provide written informed consent before study participation, according to institutional and federal guidelines. All patient record/information and image data were anonymized

and de-identified prior to retrospective analysis in this study. The eligibility criteria have been detailed previously [1]. The patient exclusion criteria included concurrent malignancies; significant medical comorbidities; significant cardiovascular disease, including uncontrolled hypertension, myocardial infarction, and unstable angina; New York Heart Association grade 2 or greater congestive heart failure; prolongation of QTc of more than 450 msec in screening ECG or history of familial long QT syndrome; a history of bleeding; proteinuria at baseline (more than 2 g/d); pregnancy or lactation; CNS metastases; or an inability to provide written informed consent. A total of 34 patients with histologically confirmed advanced HCC were enrolled. Fourteen of these patients were subsequently excluded because DCE-MRI data were not retrievable for this perfusion study; thus, 20 patients were included in the current study. This study cohort included 18 men and 2 women (age range, 30–79 years; mean age, 59.55 years). Full details of the clinical data of these patients have been reported in [1].

DCE-MRI

Pretreatment DCE-MRI of the liver was performed with a 1.5 Tesla MRI system with a phased array body coil (Avanto; Siemens, New York, NY). First, a coronal T1-weighted three-dimensional (3D) volumetric interpolated breath-hold examination (VIBE) sequence of varying flip angles of 10, 15, 30, 60, and 90 degrees was performed before CA injection. Thereafter, a total of 0.1 mmol/kg bodyweight of the CA, gadolinium-diethylenetriaminepentaacetic acid (Gd-DTPA) (Magnevist; Berlex, Montville, NJ) was injected at 2 mL/sec, followed by a saline chase of 20 mL at a rate of 2 mL/sec through a 20-gauge peripheral intravenous line in the arm. A series of coronal T1-weighted 3D VIBE images was obtained after a 5-second delay following the initiation of CA injection, and the scanning was continued for up to 4 minutes and 30 seconds. The acquisition parameters were as follows: TR = 5 msec, TE = 1.58 msec, 5-mm slice thickness, 0-mm interslice gap, 20 slices, 352×384 matrix, 15-degree flip angle, and field of view of 366×400 mm. Two consecutive 7-second acquisitions were repeated 10 times with a delay of 21 seconds between them. The scanning time of every acquisition was 14 seconds with breath holding, followed by a break of 21 seconds.

Data Processing

An image post-processing algorithm was coded in C/C++ with Visual Studio 2010 Professional Edition (Microsoft, Redmond, WA, USA). Anonymized DCE-MRI data were imported into our in-house software program and were analyzed offline by use of five different WX tracer kinetic models: the Tofts-Kety (WX-TK) model [13] based on a two-site-exchange (2SX) model for transcytolemmal exchange [14], and the extended TK (WX-ETK) model [15], two compartment exchange (WX-2CX) model [16,17], adiabatic approximation to the tissue homogeneity (WX-AATH) model [18,19], and distributed parameter (WX-DP) model [20,21] based on a three-site-two-exchange (3S2X) model for transendothelial and transcytolemmal water exchange [9] (see S1 Appendix). These models provided the following parameters: total hepatic blood flow (*BF*, mL/min/100 g), arterial flow fraction (γ), arterial blood flow (BF_A, mL/min/100 g), portal blood flow (BF_{PV}, mL/min/100 g), blood volume (*BV*, mL/100 g), mean transit time (*MTT*, min), capillary wall permeability-surface area product (*PS*, mL/min/100 g), fractional interstitial volume (v_I), extraction fraction (*E*), mean intracellular water molecule lifetime (τ_C, sec), and fractional intracellular volume (v_C). A list of the various parameters and their definitions is provided in Table 1.

For each patient, the region of interest (ROI) of a primary HCC lesion was outlined by an oncologic surgeon [K.H., with 10 years of experience in abdominal CT/MRI interpretation] in the central portions of the imaging volume for reducing inflow effects and wrap-around

Table 1. Symbols and definitions for kinetic parameters.

Term	Definition	Unit of Measure
C_A	Arterial blood concentration of tracer	g/mL
C_{PV}	Portal blood concentration of tracer	g/mL
$\overline{C}_p$	Mean concentration of tracer in the plasma compartment	g/mL
$\overline{C}_I$	Mean concentration of tracer in the interstitial compartment	g/mL
C_T	Concentration of tracer in tissue	g/mL
E_A	Relative signal enhancement in artery	None
E_{PV}	Relative signal enhancement in portal vein	None
E_T	Relative signal enhancement in tissue	None
R_T	Tissue residue function	None
Q_P	Impulse response function of the plasma compartment	mL/min/mL
Q_I	Impulse response function of the interstitial compartment	mL/min/mL
Q_T	Impulse response function of the tissue	mL/min/mL
F	Total hepatic plasma flow	mL/min
γ	Arterial flow fraction	None
F_A	Arterial plasma flow	mL/min
F_{PV}	Portal plasma flow	mL/min
BF	Total hepatic blood flow	mL/min/100 g
BF_A	Arterial blood flow	mL/min/100 g
BF_{PV}	Portal blood flow	mL/min/100 g
BV	Blood volume	mL/100 g
MTT	Mean transit time	min
PS	Capillary wall permeability-surface area product	mL/min (or mL/min/100 g)
PS_C	Cell membrane permeability-surface area product	mL/min (or mL/min/100 g)
v_B	Fractional blood volume	None
v_P	Fractional plasma volume	None
v_I	Fractional interstitial volume	None
v_C	Fractional intracellular volume	None
E	Extraction fraction	None
H_{LV}	Hematocrit in major (large) vessels	None
H_{SV}	Hematocrit in small vessels	None
M	Tissue mass	g
ρ_T	Tissue density	g/cm^3
V_P	Volume of the plasma compartment	mL
V_I	Volume of the interstitial compartment	mL
V_C	Volume of the intracellular compartment	mL
V_T	Tissue volume	mL
F/V_T	Total hepatic perfusion	mL/min/mL
F_A/V_T	Arterial perfusion	mL/min/mL
F_{PV}/V_T	Portal perfusion	mL/min/mL
$K^{Trans} = EF/V_T$	Volume transfer constant between the plasma and interstitial compartments	mL/min/mL
V_P/F	Capillary transit time	min
V_P/PS	Capillary leakage time	min
$t_{Lag,T}$	Difference in bolus arrival time between C_A (or C_{PV}) and C_T	min
τ_B	Mean intravascular water molecule lifetime	sec

(*Continued*)

Table 1. (*Continued*)

Term	Definition	Unit of Measure
τ_I	Mean intrainterstitial water molecule lifetime	sec
τ_C	Mean intracellular water molecule lifetime	sec
K_{BI}	Blood-to-interstitium water transfer rate	sec^{-1}
K_{IB}	Interstitium-to-blood water transfer rate	sec^{-1}
K_{CI}	Cell-to-interstitium water transfer rate	sec^{-1}
K_{IC}	Interstitium-to-cell water transfer rate	sec^{-1}

doi:10.1371/journal.pone.0136725.t001

artifacts. Additional ROIs (mean size: 5.2 mm^2) were placed within the aorta and the major portal vein branch for each patient, and a dual-input approach was used for analysis of the DCE-MR images [22]. The arterial input function (AIF) and the portal-venous input function (PVIF) were fitted by use of a sums-of-exponentials model [23] that describes the first-pass and recirculating inputs (see S1 Appendix). The tissue enhancement curve $E_T(t)$ for each voxel within the tumor ROIs was fitted separately with the five WX models. For mitigating a potential error in parameter estimation due to the discrete approximation of the continuous formula of the tissue concentration-time curve $C_T(t)$ [24,25], an analytic solution for $C_T(t)$ for each model was derived by incorporation of the AIF and PVIF models (see S1 Appendix). Model fitting was performed by use of a constrained nonlinear optimization algorithm based on MINPACK-1 [26] that yields the sum of squared residues as a measure of the goodness of fit, and allows upper and lower bounding constraints to be placed on each parameter [27].

To account for the difference in bolus arrival time between the various parts of the liver and the combined input (i.e., AIF and PVIF), an additional parameter $t_{Lag,T}$ (min) was included in the expression for $C_T(t)$ so that an adjustable delay was imposed relative to the dual input. The mean parameter value in the tumor ROI was taken as the representative parameter value for the tumor.

Antiangiogenic Treatment

The treatment schedule and dose modification schema have been detailed previously [1]. Briefly, patients received sunitinib at a dose of 37.5 mg daily by mouth for 4 weeks, followed by 2 weeks of rest, in 6-week cycles. Patients with grade 3 or 4 toxicities underwent dose reduction to 25 or 12.5 mg daily, respectively. Treatment was continued until progression, unacceptable toxicity, or withdrawal of consent. Patients were followed until death; one patient was alive at the end of the study, and thus the patient was censored. For this patient cohort, the median survival time was 11.42 months.

Statistical Analysis

OS was defined as the time from the start of treatment to the date of death or of the last follow-up. Because the median survival time of patients was 11.42 months (i.e., approximately one year), and this value divides the study population into two balanced survival groups, the survival risk was estimated as one year. For each model and each kinetic parameter, the optimal parameter cut-off (threshold) value for predicting 1YS was estimated by means of receiver operating characteristic (ROC) analysis [28,29]. Because the sample size was small, a leave-one-out cross-validation (LOOCV) method, which is known to provide an unbiased estimate even in case of small samples [28,29] was used in the ROC analysis as follows: At each iteration of the LOOCV method, one of the patients was left out, and the parameter values of the

remaining patients were subjected to the ROC analysis over the two survival groups of patients for generating an ROC curve. The point closest to the top-left corner on the ROC curve, i.e., the point that provides min{(1−sensitivities)^2 + (1−specificities)^2}, was identified as a parameter cut-off value. At the end of each iteration, the left-out patient was categorized into either the "low-risk" or "high-risk" group based on the parameter cut-off value. This process of ROC curve and cut-off value estimation was repeated at each LOOCV iteration, until all of the patients had been left out once and categorized to either the low-risk or high-risk group. Finally, after the LOOCV iterations had been completed, the cut-off value that had the highest frequency during the LOOCV iterations was identified as an optimal cut-off value for the parameter, and Kaplan-Meier analysis with log-rank test was performed for comparing the two groups generated during the LOOCV iterations.

Kaplan-Meier survival curves for patients in the low- and high-risk groups were constructed for display of the proportion of patients alive at any given time. The statistical significance in the difference between these Kaplan-Meier curves was evaluated by use of the log-rank statistic and its permutation-based significance test [29], in which 1000 random permutations were performed and the associated *P* values were calculated.

For association of a kinetic parameter with OS, univariate Cox proportional hazard regression analysis concerning the continuous parameter values was performed for testing of individual kinetic parameters for each WX kinetic model. For each parameter, *P* values were computed based on 1000 random permutations. The hazard ratio (HR) was defined as the ratio of hazards for a two-fold change in the parameter values. The HR was equal to exp(b), where b is the Cox regression coefficient. Statistical analyses were performed by use of statistical software R (version 3.0.1) and BRB-ArrayTools (version 4.4.0) [30–32].

Results

Examples of fitting of the five different WX dual-input tracer kinetic models to a voxel-level enhancement curve within HCC, the fitted $E_T(t)$, and the corresponding impulse response function $Q_T(t)$ are shown in Fig 1. Fig 2 shows two examples of cases from each of the high- and low-risk groups, with voxel-level fittings and parameter maps generated by use of the five WX models. Table 2 summarizes the mean values for the different parameters for the different WX models.

One-year Survival

Table 3 shows the optimized cut-off values of the parameters determined by ROC analysis with LOOCV for each model along with the *P* values for the log-rank permutation test. For the WX-2CX, WX-AATH and WX-DP model, the cross-validated Kaplan-Meier curves were not significantly different between the two groups ($P>0.05$). Only the WX-TK-model-derived γ and v_I, and the WX-ETK-model-derived τ_C and v_C were significant biomarkers for 1YS (Fig 3). The WX-TK-model-derived γ and v_I were both lower in the high-risk than in the low-risk group, with cut-off values of 0.733 ($P = 0.022$) and 0.300 ($P = 0.010$), respectively. The WX-ETK-model-derived τ_C and v_C were both higher in the high-risk than in the low-risk group, with cut-off values of 0.927 sec ($P = 0.023$) and 0.611 ($P = 0.042$), respectively.

Overall Survival

Table 4 shows the hazard ratios and corresponding *P* values for the parameters determined by the univariate Cox proportional hazard model for each kinetic model. The results showed that the WX-TK (HR = 21.51, $P = 0.034$), WX-ETK (HR = 8.418, $P = 0.038$), WX-AATH (HR = 10.14, $P = 0.028$), and WX-DP-model-derived v_C (HR = 4.213, $P = 0.041$), and the

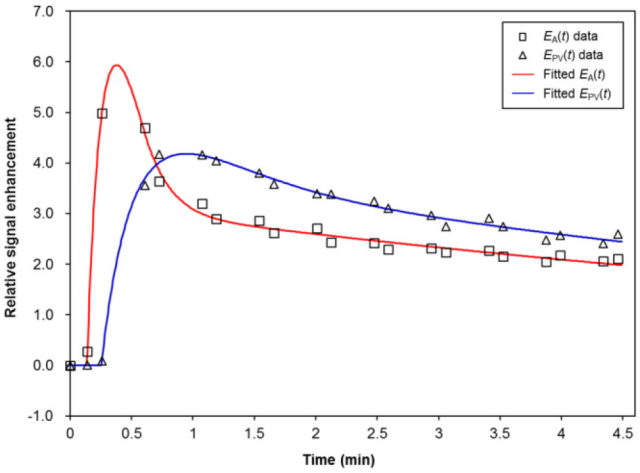
$E_A(t)$ data
$E_{PV}(t)$ data
Fitted $E_A(t)$
Fitted $E_{PV}(t)$
Relative signal enhancement
Time (min)

a.

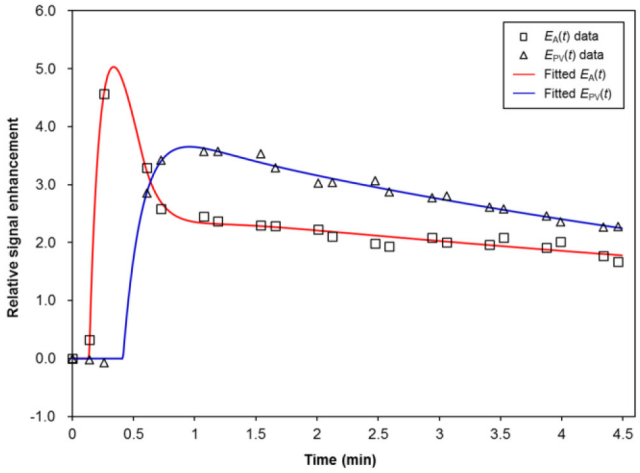
$E_A(t)$ data
$E_{PV}(t)$ data
Fitted $E_A(t)$
Fitted $E_{PV}(t)$
Relative signal enhancement
Time (min)

b.

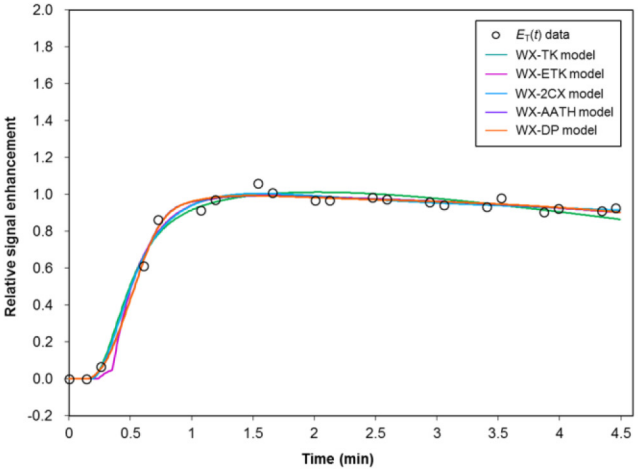
$E_T(t)$ data
WX-TK model
WX-ETK model
WX-2CX model
WX-AATH model
WX-DP model
Relative signal enhancement
Time (min)

c.

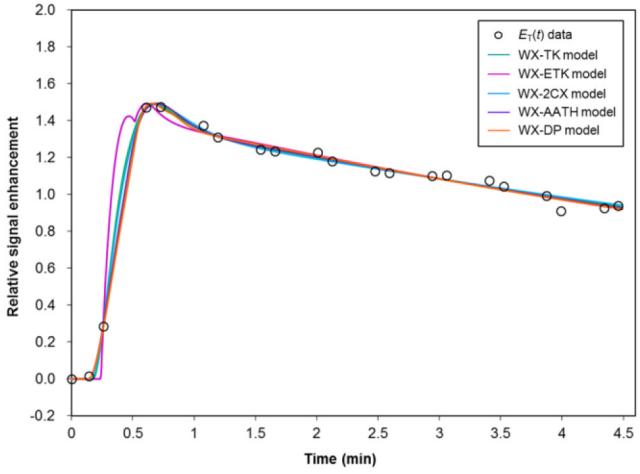
$E_T(t)$ data
WX-TK model
WX-ETK model
WX-2CX model
WX-AATH model
WX-DP model
Relative signal enhancement
Time (min)

d.

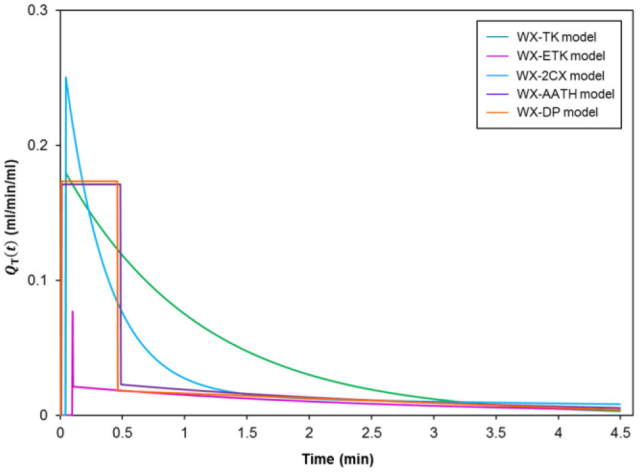
WX-TK model
WX-ETK model
WX-2CX model
WX-AATH model
WX-DP model
$Q_T(t)$ (ml/min/ml)
Time (min)

e.

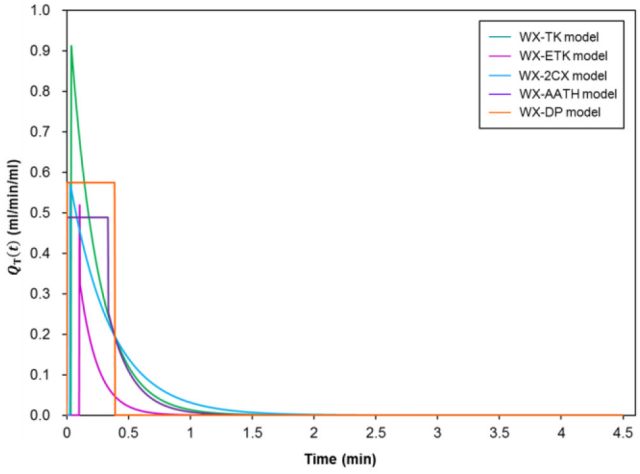
WX-TK model
WX-ETK model
WX-2CX model
WX-AATH model
WX-DP model
$Q_T(t)$ (ml/min/ml)
Time (min)

f.

Fig 1. Example of fitting of arterial and portal-venous curves and tissue enhancement curves with various models. Graphs illustrate examples of (A and B) fitting of the arterial and portal input enhancement curves, (C and D) fitting of the five different models to a voxel enhancement curve which was sampled from the HCC, and (E and F) their corresponding impulse response curves (i.e., $Q_T(t) = (F/V_T) \cdot R_T(t)$) where two different cases are shown in the left and right columns. WX = water-exchange-modified, TK = Tofts-Kety, ETK = extended Tofts-Kety. 2CX = two compartment exchange, AATH = adiabatic approximation to tissue homogeneity, and DP = distributed parameter.

doi:10.1371/journal.pone.0136725.g001

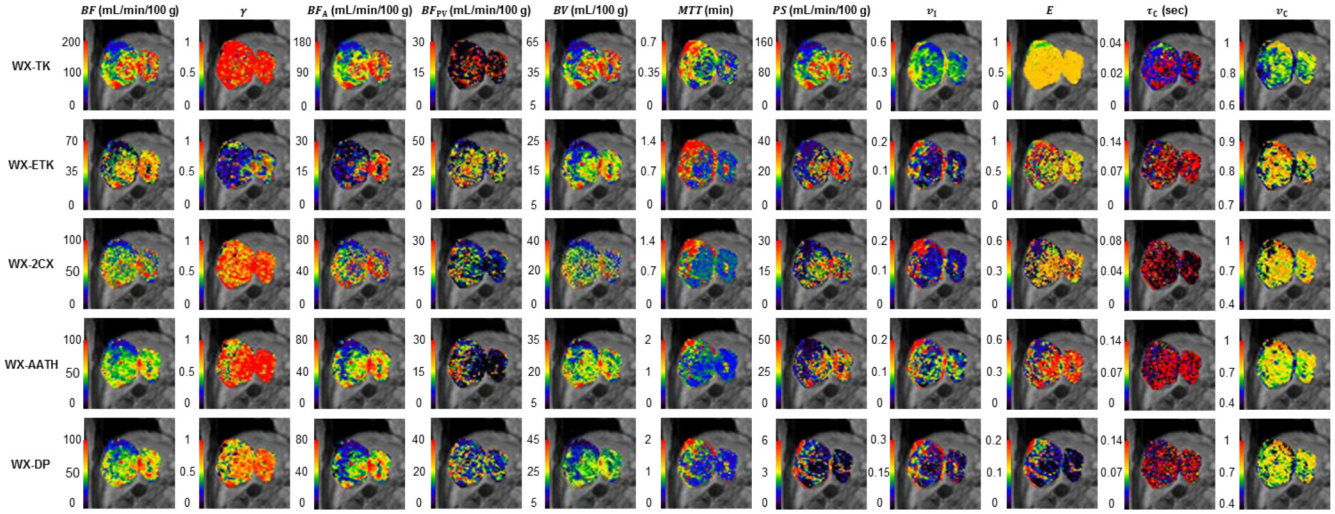

a.

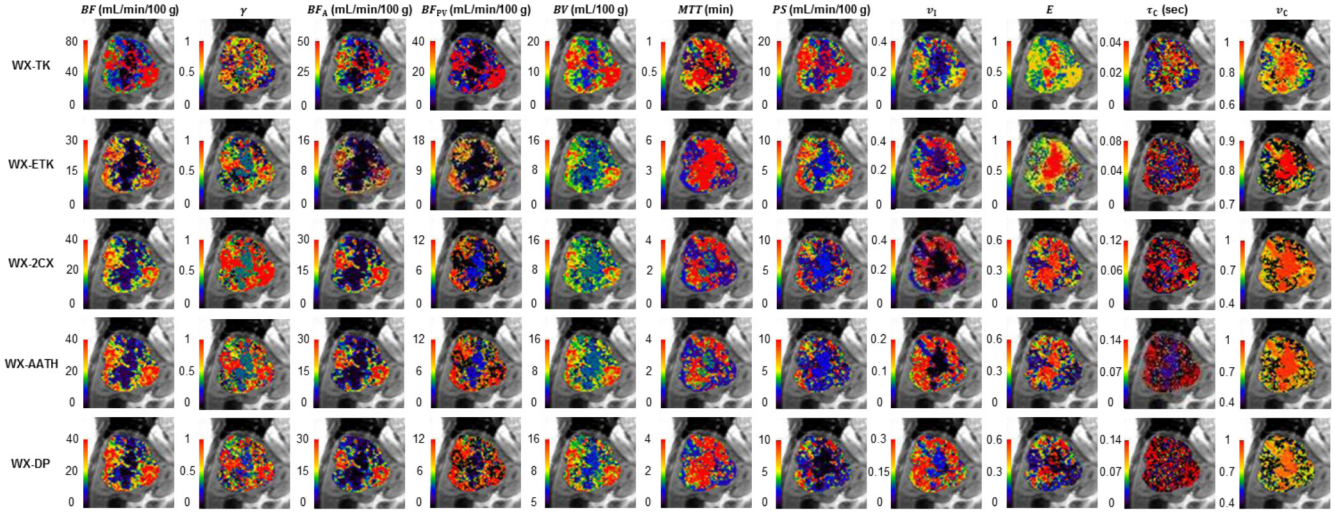

b.

Fig 2. Example of kinetic parameter maps derived from various models. Parametric maps of total hepatic blood flow (*BF*), arterial flow fraction (γ), arterial blood flow (BF_A), portal blood flow (BF_{PV}), blood volume (*BV*), mean transit time (*MTT*), capillary wall permeability-surface area product (*PS*), fractional interstitial volume (v_I), extraction fraction (*E*), mean intracellular water molecule lifetime (τ_C), and fractional intracellular volume (v_C) for HCC in (A) a low-risk man aged 52 years who survived for 23.87 months, and (B) a high-risk man aged 72 years who survived for 8.53 months. WX = water-exchange-modified, TK = Tofts-Kety, ETK = extended Tofts-Kety, 2CX = two compartment exchange, AATH = adiabatic approximation to tissue homogeneity, and DP = distributed parameter.

doi:10.1371/journal.pone.0136725.g002

Table 2. Parameter values derived from the five different WX kinetic models.

Parameter	Mean ± SD for high- and low-risk populations				
	WX-TK	WX-ETK	WX-2CX	WX-AATH	WX-DP
BF	133.4 ± 86.17	36.74 ± 21.78	49.94 ± 26.89	49.20 ± 24.17	53.47 ± 28.13
γ	0.702 ± 0.255	0.459 ± 0.220	0.730 ± 0.256	0.637 ± 0.284	0.517 ± 0.263
BF_A	95.36 ± 81.05	17.56 ± 17.90	38.71 ± 27.23	33.50 ± 22.58	29.44 ± 22.88
BF_{PV}	38.09 ± 39.04	19.18 ± 13.51	11.23 ± 14.95	15.70 ± 15.34	24.03 ± 18.35
BV	46.10 ± 27.61	18.45 ± 9.339	17.89 ± 8.733	18.97 ± 8.092	21.01 ± 10.35
MTT	1.315 ± 2.066	4.605 ± 2.739	2.212 ± 1.916	1.817 ± 1.583	2.398 ± 2.768
PS	98.42 ± 66.30	31.63 ± 22.40	16.22 ± 10.58	20.03 ± 12.42	5.452 ± 3.649
v_I	0.257 ± 0.091	0.171 ± 0.076	0.181 ± 0.108	0.163 ± 0.073	0.220 ± 0.088
E	0.606 ± 0.057	0.651 ± 0.104	0.346 ± 0.136	0.407 ± 0.119	0.197 ± 0.183
τ_C	0.871 ± 0.684	1.050 ± 0.521	0.657 ± 0.645	1.212 ± 0.977	0.657 ± 0.627
v_C	0.743 ± 0.091	0.637 ± 0.111	0.633 ± 0.139	0.639 ± 0.114	0.561 ± 0.146
RMSE	0.179 ± 0.126	0.152 ± 0.092	0.160 ± 0.108	0.151 ± 0.101	0.168 ± 0.128

Note.—SD = standard deviation, WX = water-exchange-modified, TK = Tofts-Kety, ETK = extended Tofts-Kety, 2CX = two compartment exchange, AATH = adiabatic approximation to the tissue homogeneity, DP = distributed parameter, *BF* = total hepatic blood flow (in mL/min/100 g), γ = arterial flow fraction (unitless), BF_A = arterial blood flow (in mL/min/100 g), BF_{PV} = portal blood flow (in mL/min/100 g), *BV* = blood volume (in mL/100 g), *MTT* = mean transit time (in min), *PS* = capillary wall permeability-surface area product (in mL/min/100 g), v_I = fractional interstitial volume (unitless), *E* = extraction fraction (unitless), τ_C = mean intracellular water molecule lifetime (sec), v_C = fractional intracellular volume (unitless), and *RMSE* = root-mean-square error between original and fitted $E_T(t)$.

doi:10.1371/journal.pone.0136725.t002

WX-DP-model-derived BF_A (HR = 0.716, $P = 0.025$), were associated with OS, indicating that the risk of death rises by approximately 35.9%, 23.7%, 26.1%, and 15.5% for an increase of 0.1

Table 3. Optimal cut-off values of parameters and their log-rank test results from leave-one-out cross-validated Kaplan-Meier analysis in terms of 1-year survival.

Parameter	Cut-off value (*P*-value)				
	WX-TK	WX-ETK	WX-2CX	WX-AATH	WX-DP
BF	111.5 (0.345)	36.66 (0.315)	56.04 (0.220)	56.23 (0.315)	59.22 (0.682)
γ	0.833 (**0.022**)*	0.475 (0.871)	0.763 (0.277)	0.591 (0.338)	0.572 (0.080)
BF_A	47.19 (0.172)	12.09 (0.359)	39.18 (0.662)	36.42 (0.952)	28.58 (0.662)
BF_{PV}	10.45 (0.776)	23.99 (0.447)	5.592 (0.233)	10.36 (0.795)	15.03 (0.491)
BV	37.27 (0.345)	16.89 (0.315)	20.66 (0.379)	21.30 (0.168)	18.69 (0.634)
MTT	0.380 (0.442)	5.575 (0.597)	1.709 (0.341)	1.333 (0.163)	1.414 (0.163)
PS	80.52 (0.504)	26.31 (0.315)	19.95 (0.725)	20.04 (0.644)	2.697 (0.782)
v_I	0.300 (**0.010**)*	0.123 (0.161)	0.207 (0.344)	0.142 (0.206)	0.209 (0.460)
E	0.603 (0.682)	0.635 (0.981)	0.298 (0.367)	0.413 (0.224)	0.118 (0.377)
τ_C	0.482 (0.199)	0.927 (**0.023**)*	0.376 (0.831)	0.819 (0.588)	0.284 (0.702)
v_C	0.728 (0.131)	0.611 (**0.042**)*	0.533 (0.282)	0.646 (0.468)	0.518 (0.194)

Note.—WX = water-exchange-modified, TK = Tofts-Kety, ETK = extended Tofts-Kety, 2CX = two compartment exchange, AATH = adiabatic approximation to the tissue homogeneity, DP = distributed parameter, *BF* = total hepatic blood flow (in mL/min/100 g), γ = arterial flow fraction (unitless), BF_A = arterial blood flow (in mL/min/100 g), BF_{PV} = portal blood flow (in mL/min/100 g), *BV* = blood volume (in mL/100 g), *MTT* = mean transit time (in min), *PS* = capillary wall permeability-surface area product (in mL/min/100 g), v_I = fractional interstitial volume (unitless), *E* = extraction fraction (unitless), τ_C = mean intracellular water molecule lifetime (sec), and v_C = fractional intracellular volume (unitless). Bold numbers with asterisk (*) indicate a statistically significant difference in the 1000 log-rank permutation test (two-sided $P<0.05$).

doi:10.1371/journal.pone.0136725.t003

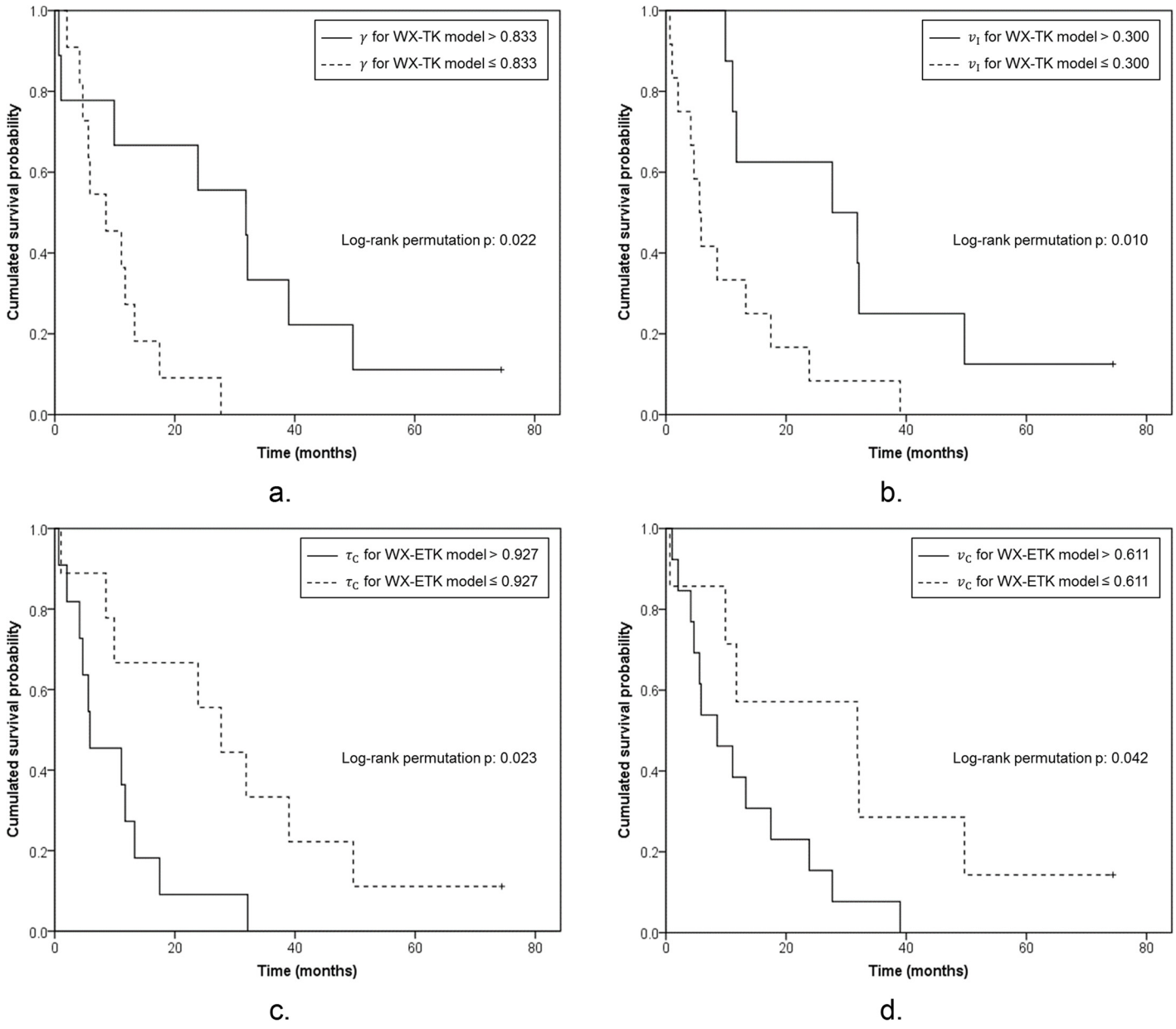

Fig 3. Kaplan-Meier curves for kinetic parameters predictive of 1-year survival. Cross-validated Kaplan-Meier plots for (A) arterial flow fraction (γ) and (B) fractional interstitial volume (v_I) derived from the water-exchange-modified Tofts-Kety (WX-TK) model, and (C) mean intracellular water molecule lifetime (τ_C) and (D) fractional intracellular volume (v_C) derived from the water-exchange-modified extended Tofts-Kety (WX-ETK) model. Survival of patients with advanced HCC treated with sunitinib was better with γ over 0.833 and v_I over 0.300 in the WX-TK model, and with τ_C at most 0.927 sec and v_C at most 0.611 in the WX-ETK model.

doi:10.1371/journal.pone.0136725.g003

(10%) in the WX-TK, WX-ETK, WX-AATH, and WX-DP-model-derived v_C, respectively, and falls by 28.4% for an increase of 1 mL/min/100 g in the WX-DP-model-derived BF_A.

Overall, the WX-ETK-model-derived v_C was not only identified as a statistically significant prognostic biomarker for 1YS, but was also statistically significantly associated with OS.

Table 4. Results of univariate Cox's proportional hazards regression analysis of parameters in terms of overall survival.

Parameter	Hazard ratio (*P*-value)				
	WX-TK	WX-ETK	WX-2CX	WX-AATH	WX-DP
BF	0.785 (0.217)	0.747 (0.138)	0.717 (0.076)	0.680 (0.092)	0.693 (0.092)
γ	0.879 (0.562)	0.961 (0.890)	0.927 (0.747)	0.843 (0.376)	0.792 (0.198)
BF_A	0.753 (0.063)	0.796 (0.203)	0.757 (0.093)	0.734 (0.051)	0.716 (**0.025**)*
BF_{PV}	1.183 (0.248)	0.930 (0.564)	1.012 (0.914)	1.049 (0.760)	1.076 (0.684)
BV	0.805 (0.362)	0.687 (0.218)	0.660 (0.055)	0.557 (0.069)	0.642 (0.110)
MTT	1.247 (0.166)	1.125 (0.695)	1.356 (0.165)	1.371 (0.180)	1.275 (0.266)
PS	0.816 (0.272)	0.815 (0.307)	0.756 (0.173)	0.747 (0.195)	0.959 (0.829)
v_I	0.438 (0.053)	0.660 (0.307)	0.942 (0.788)	0.660 (0.332)	0.577 (0.196)
E	1.975 (0.804)	1.656 (0.612)	1.331 (0.541)	1.322 (0.694)	1.181 (0.373)
τ_C	0.821 (0.424)	1.353 (0.415)	1.237 (0.326)	1.031 (0.883)	1.053 (0.828)
v_C	21.51 (**0.034**)*	8.418 (**0.038**)*	4.109 (0.094)	10.14 (**0.028**)*	4.213 (**0.041**)*

Note.—WX = water-exchange-modified, TK = Tofts-Kety, ETK = extended Tofts-Kety, 2CX = two compartment exchange, AATH = adiabatic approximation to the tissue homogeneity, DP = distributed parameter, *BF* = total hepatic blood flow (in mL/min/100 g), γ = arterial flow fraction (unitless), BF_A = arterial blood flow (in mL/min/100 g), BF_{PV} = portal blood flow (in mL/min/100 g), *BV* = blood volume (in mL/100 g), *MTT* = mean transit time (in min), *PS* = capillary wall permeability-surface area product (in mL/min/100 g), v_I = fractional interstitial volume (unitless), *E* = extraction fraction (unitless), τ_C = mean intracellular water molecule lifetime (sec), and v_C = fractional intracellular volume (unitless). Bold numbers with asterisk (*) indicate a statistically significant difference in the 1000 permutation test for hazard ratio in univariate Cox proportional hazards analysis (two-sided $P<0.05$).

doi:10.1371/journal.pone.0136725.t004

Discussion

Several studies have assessed the impact of water exchange on the estimation of pharmacokinetic parameters, but no definite conclusions have been reached about the significance of water exchange effects in clinical practice. Bains *et al.* analyzed DCE-MRI data by using the WX-2CX model under the FXL and no-exchange-limit conditions, and they compared kinetic parameters derived from DCE-MRI with those obtained from exchange-insensitive DCE-CT in bladder cancer [33]. They concluded that the cell-to-interstitium water transfer rate (K_{CI}) has a negligible effect on estimates of kinetic parameters, whereas the blood-to-interstitium water transfer rate (K_{BI}) influences estimates of the fractional plasma volume (v_P). Huang *et al.* compared the FXL standard and shutter-speed (fast-exchange regime) approaches of the TK model, and they demonstrated that relieving of the FXL constraint leads to a higher performance for breast cancer diagnosis [11]. Using computer simulations in the WX-ETK model, Paudyal *et al.* demonstrated that the effect of a variation of K_{BI} is significant for v_P and is minimal for the transfer constant ($K^{Trans} = EF/V_T$) and the fractional interstitial volume (v_I) when K_{CI} is held constant, whereas K^{Trans} and v_I are influenced by a variation in K_{CI} when K_{BI} is held constant [34]. Using simulated DCE-MRI data, Zhang and Kim assessed four different kinetic models (FXL standard ETK, shutter-speed ETK, FXL standard AATH, and WX-AATH models), and they found that K^{Trans}, v_I, and v_P values estimated from the WX-AATH model had the highest accuracy [35]. Because the rate of water exchange is related to the cell type, size, shape, and membrane permeability [10], the vascular-interstitial and cellular-interstitial water exchange can vary significantly between normal and tumor tissue [36]. Therefore, DCE-MRI yields a variety of water exchange regimes, and here we focused on a water exchange paradigm based on a full 2SX model [14] or a full 3S2X model [34] that can fully describe the effects from fast to intermediate or slow water exchange (see S1 Appendix). To the authors' knowledge, this is the first comparative study that identified a prognostic WX tracer kinetic model and parameter for 1YS and OS of patients with advanced HCC who received sunitinib monotherapy.

Our results showed that the WX-ETK-model-derived v_C was identified as the most effective prognostic biomarker for OS and 1YS, which was higher in the high-risk than in the low-risk group. We assume that these results are associated with tumor hypoxia. Although HCC is a highly angiogenic cancer, it is also characterized by hypoxia that promotes HCC growth, progression, angiogenesis, and resistance to therapies [37]. Thus, the high-risk patients may have relatively more hypoxic HCC [38]. In a hypoxic environment, the mitochondrial oxygen consumption rate and adenosine triphosphate (ATP) production are reduced, which hinders inter alia active transport into tumor cells [39]. The reduction of ATP by a decreased oxygen supply causes disturbances in membrane ion translocation that result in cell swelling, which may induce high v_C [40]. On the other hand, Heider et al. [41] demonstrated that the tumor blood flow was correlated positively with tumor oxygenation in a CT perfusion study of cervical cancer. Thus, it is assumed that low tumor BF_A is associated with a hypoxic tumor microenvironment, which leads to poor-outcome-promoting oncogenic mutations, cell survival, and more aggressive behavior of tumors [42]. Besides, low tumor BF_A, which leads the disturbed microcirculation of antiangiogenic agents and the deterioration of their diffusion conditions, may result in poor OS of HCC patients treated with sunitinib [12,39,43].

Our results also showed that the parameters that were found to be statistically significant prognostic biomarkers for 1YS (the WX-TK-model-derived γ and v_I) were not necessarily statistically significantly associated with OS. In contrast, the WX-DP-model-derived BF_A, and the WX-TK, WX-AATH and WX-DP-model-derived v_C were not statistically significant prognostic biomarkers for 1YS, although they were statistically significantly associated with OS. The time scale for events can be classified as either continuous or discrete, and the methods applied to one type of time scale do not necessarily apply to the other [44]. A fundamental problem with methods based on dividing the timeline into discrete intervals is the loss of information. Therefore, our results suggest that analyzing both continuous- and discrete-time events may be necessary for finding a robust prognostic biomarker.

As antiangiogenic agents might exert different pharmacokinetic effects on tumor flow and permeability, a method that can separately estimate the plasma flow F (in mL/min) and PS may be of central importance for understanding tissue hemodynamics. The early version of the TK model, which has been used most frequently, facilitates the extraction of the volume transfer constant K^{Trans} (in min^{-1}), the physiologic interpretation of which reflects a combination of F and PS [15], but it has been known that their separate estimates are impossible with the TK model. The relative magnitude of PS and F determines E, i.e., the fraction of the mass of CA arriving at the tissue which leaks into the interstitial space in a single passage through the vasculature.

Under the mixed flow- and permeability-limited condition, $K^{Trans} = EF/V_T$ [13,15], where V_T is the examined tissue volume (in mL), and F/V_T is the tissue perfusion (in mL/min/mL). With further assumption that $v_P \ll v_I$, a single compartment TK model can be derived (see S1 Appendix). The original TK model additionally presumed that CA in the plasma compartment can be neglected (i.e., $v_P \cong 0$) [45]. However, a separate determination of E and F/V_T is impossible with the assumption that $v_P \cong 0$. In this study, we refined the TK model parameterization so that K^{Trans} was decomposed into E and F/V_T, by assuming that $v_P \ll v_I$. The assumption of $v_P \ll v_I$ leads to $C_T(t) \cong v_I C_I(t)$, where $C_I(t)$ is the CA concentration in the interstitial compartment, and thereby the capillary transit time V_P/F (in min) and the capillary leakage time V_P/PS (in min) are negligible, where $V_P = v_P V_T$ is the plasma volume (in mL). However, their reciprocals, F/V_P (in mL/min/mL) and PS/V_P (in mL/min/mL), are both infinite if $v_P \cong 0$. Because F and PS cannot be calculated without v_P (i.e., E becomes undefined), the assumption that $v_P \cong 0$ may contradict with the original TK model. On the other hand, if $v_P \neq 0$, then F/V_P and PS/V_P are finite, and thus $F/V_T = v_P F/V_P = v_I F/V_I$ and $PS/V_T = v_P PS/V_P = v_I PS/V_I$, where $V_I = v_I V_T = (v_I/v_P)V_P$

is the interstitial volume (in mL), are not only calculable, but also E can be defined (e.g., $E = 1 - e^{-(PS/V_P)/(F/V_P)}$). As a result, F and PS can be measured separately with our new parameterization rules of the TK model. These parameterization rules, which have originally been proposed by Brix *et al.* for evaluation of the 2CX model [16], apply to all of the kinetic models considered in this study (see S1 Appendix), and the enable fair comparisons among different kinetic models. Even if parameterization rules are different between the original approaches and our methods on tracer kinetic modeling, the mass balance principle of CA in the capillary-tissue system is identical for them.

To date, very few data have been reported on the issue of limited vascular-interstitial water exchange and its effect on DCE-MRI. Here, we assumed that the vascular-interstitial exchange behavior would virtually be identical between the CA (Gd-DTPA) and water molecules (see S1 Appendix). In the absence of the CA, water exchange is usually regarded as being in the FXL [8,14], but in its presence, it enters the interstitium from the plasma and increases the relaxation rate of interstitial water while the T1 of water in the cell remains the same, which may lead to significant transient sorties away from the precontrast water exchange state. Even though water molecules are much lighter (≅18 g/mol) than Gd-DTPA molecules (Magnevist, 938 g/mol), and the self-diffusion coefficient of water ($D = 2.2 \times 10^{-9}$ m^2/sec) is higher than that of Gd-DTPA (Magnevist, $D = 2.6 \times 10^{-10}$ m^2/sec) [46], it should be noted that slow or fast water exchange does not refer directly to the speed with which the water molecule moves between the two spaces, but to the ratio of this motion to the difference in relaxation rates of the two spaces [47]. If the two spaces have identical relaxation rates, they will always be described as being in the FXL but slowly the water molecules exchange between them, because no distinction can be made between their relaxation properties. Contrarily, if the two spaces have an order-of-magnitude difference in their each relaxation rates, they will be in the slow exchange regime even though water moves very rapidly between them, because their relaxation properties will always be the major focus of the decision of water exchange [48].

The addition of CA to the interstitial space does not change the motion of water molecules, but it increases the intrinsic relaxation rate of the interstitial space. Given the large difference in relaxation rates in the two spaces immediately after the CA injection, the water exchange would significantly depart from the FXL, because the CA might not have had time to pass into the interstitial space while being present in high concentration in the intravascular space. For example, with an intact blood-brain barrier that has very low permeability, the vascular-interstitial water exchange slowly approaches the limit during the first pass of a bolus of Gd-DTPA [49]. On the other hand, if the CA enters the interstitial space quickly, the effect of slow water exchange is short-lived. For example, in the heart, where the first-pass extraction of Gd-DTPA is significant, the slow-water-exchange effect decreases quickly [49]. As such, the vascular-interstitial water exchange with typical CA concentrations is in the slow- to intermediate-exchange regime [8], and the trends in water mobility to the difference in relaxation rates of the two spaces seem to be more like Gd-DTPA exchange behavior rather than the inherent speed of movement of the water. Furthermore, even if the vascular-interstitial water exchange rates may appear to be faster in tumors where the vascular permeability is larger, they are probably dependent on the geometric and hemodynamic heterogeneity of microvascular networks as well as the microvascular permeability.

HCC is a heterogeneous disease with multiple etiologies that has an abnormal blood flow and is excessively leaky [38]. Setting the water exchange rate to a value reported in the literature is unlikely to reflect a complex phenomenon involving multiple exchange behaviors in the context of a spatially heterogeneous tumor microenvironment. As an alternative, model fitting can be done by considering the mean intravascular water molecule lifetime τ_B as an additional free

parameter independent from the exchange rate of CA [9]. However, the accuracy and precision in such an approach may be low [35]. The reason for this is not obvious, but one could hypothesize that the estimation of τ_B might be difficult without the aid of tracer kinetic parameters because τ_B is calculated based on the ratio of BV to PS [8]. In contrast, τ_C can be used as an independent variable [14], because Gd-DTPA does not permeate the cell membrane and pass into the intracellular space, whereas the cellular-interstitial water exchange is intermediate to fast [8]. Therefore, although the speed of intercompartmental water exchange cannot be set to a single value, our approach would be a plausible implicit compromise for the evaluation of tumor angiogenesis.

When more complex models such as WX kinetic models are used for data analysis, the goodness of fit alone may not be sufficient to ensure that the estimated parameters truly reflect the corresponding biophysical properties of the tissue [35]. Therefore, in this study, we compared the prognostic ability for patient survival among different WX kinetic models under the same experimental conditions to identify clinically relevant biomarkers. Although such biomarkers may provide clinical realism and biologic validity, the precision in the parameter estimates may be influenced by the low temporal resolution of the DCE-MRI data. In addition, because the data-fitting process is formulated as an optimization task, the nonlinear characteristics of the kinetic model may lead to a convergence problem. Moreover, as DCE-MRI data are obtained sequentially at fixed time points, issues of discontinuity may arise which are caused by the initial step of the impulse residue function at the bolus arrival time (any model) and at the capillary transit time (AATH and DP models) [25]. To mitigate these problems, we first imposed upper and lower boundary constraints to the parameter values in order to avoid its over- and under-fitting. Second, we employed standard gradient-based optimization algorithms with an explicit analytic solution via continuous-time-domain convolution between the hepatic dual-input function (AIF and PVIF) and $Q_T(t)$ for each kinetic model, in which the WX dual-input kinetic models were extended include the primary (first-pass) and recirculation bolus arrival times as a free continuous parameter $t_{Lag,T}$ (see S1 Appendix).

It should also be noted that both the AIF and PVIF hold the same smooth and integrable functional forms, so that their scaling constants and bolus arrival times constrain kinetic parameter values at any temporal resolution. Therefore, the occurrences of discontinuities in the impulse residue function do not necessarily result in a discontinuous or nondifferentiable $C_T(t)$, which poses difficulties for curve-fitting algorithms employing gradient-based optimization schemes. Although some parameters such as BF, BV, and $t_{Lag,T}$ might be influenced by the low temporal resolution of the DCE-MRI data, the continuous-time analytic formulations of $C_T(t)$ would lower the potential bias in parameter estimates [25]. A more precise analysis may require a higher temporal resolution. Investigation of the impact of modifications in DCE-MRI acquisition techniques on kinetic parameters was beyond the scope of this study, although it is an important issue that deserves more thorough investigation in future studies.

Accurate estimates of v_P is clinically useful for assessing the integrity of the tumor microvasculature [50,51] and for monitoring the response to antiangiogenic therapy [52,53]. Although BV, in which the ratio BV/v_P is a constant, was not chosen as a prognostic biomarker in this study, v_P might have an influence on estimation of v_C. The FXL assumption may bias the accuracy and reproducibility of v_P measurements because of the restricted vascular-interstitial water exchange [54]. In addition, if the concentration of CA in the interstitial space were to reach a significant level, the cellular-interstitial water exchange would depart from the FXL [10,14,55]. Because the mixing phase, during which the injected bolus is mixed with the blood plasma and interstitial compartments, lasts up to about 2 minutes [45], the effects of slow cellular-interstitial water exchange would be felt during the longer total measurement time (4.5 minutes) in this study. The full 3S2X model determines kinetic parameters, including both the vascular-interstitial and cellular-interstitial water transfer rates, but the full 2SX model includes

only the cellular-interstitial water transfer rate [9]. Therefore, the fact that the full 3S2X model (WX-ETK model) outperformed the full 2SX model (WX-TK model) in this study confirms that the inclusion of the vascular-interstitial water exchange is necessary for the effective risk assessment of tumor characteristics such as vascularity, cellularity, and hypoxia.

There are limitations to our study. First, this is a retrospective analysis on a relatively small number of patients from a Phase II clinical trial, although it serves as a pilot comparative study. Second, the single-arm study design of the clinical trial did not allow us to evaluate the predictive value of the kinetic parameters as imaging biomarkers; instead, the prognostic value of the kinetic parameters was evaluated by means of statistical resampling methods. Third, the prognostic value was evaluated on the kinetic parameters only on the pretreatment DCE-MRI, because the primarily clinical goal of this study was to find a prognostic imaging biomarker that estimates the prognosis of patients before the treatment starts. Evaluation of the prognostic value of the kinetic parameters of the post-treatment DCE-MRI, which may have an effect on the 1YS and OS, remains for further study. Forth, survival risk estimation based on the selected cut-off values of the kinetic parameters with use of ROC analysis may result in an overestimate of the prognostic value of the parameters. Ideally, this type of analysis should have been performed based on large independent training and testing data sets. When the data size is not large enough, cross-validation methods are known to be more efficient than splitting of the data set into training and testing subsets [29]. We thus performed LOOCV and permutation tests to obtain an estimate of the prognostic value of the kinetic parameters. We believe that we were able to estimate a reasonably unbiased and generalizable prognostic value of the kinetic parameters with respect to 1YS as well as association with OS. Finally, the clinical value of the prognostic imaging biomarker found in this study may be limited to the patients who are treated with sunitinib monotherapy. Currently, sunitinib monotherapy is not an accepted treatment for patients with advanced HCC in clinical practice. Thus, the clinical value of the prognostic imaging biomarker for the patients treated with sorafenib, the current standard treatment, and other antiangiogenic therapies remains unknown. We believe, however, that the findings on the prognostic value of the kinetic parameters from DCE-MRI data have significant implications for antiangiogenic agents, and thus warrant further validation in larger prospective studies.

Conclusion

In conclusion, kinetic parameters derived from WX dual-input tracer kinetic models of DCE-MRI data can be effective prognostic biomarkers for survival of patients with advanced HCC. The choice of kinetic models influences the predictability of survival, and the WX-ETK-model-derived v_C was found to be an effective prognostic biomarker for both 1YS and OS in patients with advanced HCC who received sunitinib monotherapy. The fact that the v_C biomarker is available only from the WX kinetic formulation indicates that the water transport properties of cells is an important predictor of cancer cell development.

Supporting Information

S1 Appendix. Water-exchange-modified tracer kinetic modeling in DCE-MRI.
(DOCX)

Author Contributions

Conceived and designed the experiments: SHL HY. Performed the experiments: SHL KH. Analyzed the data: SHL KH HY. Contributed reagents/materials/analysis tools: SHL AXZ DVS. Wrote the paper: SHL KH AXZ HY.

References

1. Zhu AX, Sahani DV, Duda DG, di Tomaso E, Ancukiewicz M, Catalano OA, et al. Efficacy, safety, and potential biomarkers of sunitinib monotherapy in advanced hepatocellular carcinoma: a phase II study. J Clin Oncol. 2009; 27: 3027–3035. doi: 10.1200/JCO.2008.20.9908 PMID: 19470923
2. Yopp AC, Schwartz LH, Kemeny N, Gultekin DH, Gonen M, Bamboat Z, et al. Antiangiogenic therapy for primary liver cancer: correlation of changes in dynamic contrast-enhanced magnetic resonance imaging with tissue hypoxia markers and clinical response. Ann Surg Oncol. 2011; 18: 2192–2199. doi: 10.1245/s10434-011-1570-1 PMID: 21286939
3. Sahani DV, Jiang T, Hayano K, Duda DG, Catalano OA, Ancukiewicz M, et al. Magnetic resonance imaging biomarkers in hepatocellular carcinoma: association with response and circulating biomarkers after sunitinib therapy. J Hematol Oncol. 2013; 6: 51-8722-6-51. doi: 10.1186/1756-8722-6-51
4. Koh TS, Thng CH, Hartono S, Kwek JW, Khoo JB, Miyazaki K, et al. Dynamic contrast-enhanced MRI of neuroendocrine hepatic metastases: A feasibility study using a dual-input two-compartment model. Magn Reson Med. 2011; 65: 250–260. doi: 10.1002/mrm.22596 PMID: 20860001
5. Miyazaki K, Orton MR, Davidson RL, d'Arcy JA, Lewington V, Koh TS, et al. Neuroendocrine tumor liver metastases: use of dynamic contrast-enhanced MR imaging to monitor and predict radiolabeled octreotide therapy response. Radiology. 2012; 263: 139–148. doi: 10.1148/radiol.12110770 PMID: 22344403
6. Taouli B, Johnson RS, Hajdu CH, Oei MT, Merad M, Yee H, et al. Hepatocellular carcinoma: perfusion quantification with dynamic contrast-enhanced MRI. AJR Am J Roentgenol. 2013; 201: 795–800. doi: 10.2214/AJR.12.9798 PMID: 24059368
7. Bultman EM, Brodsky EK, Horng DE, Irarrazaval P, Schelman WR, Block WF, et al. Quantitative hepatic perfusion modeling using DCE-MRI with sequential breathholds. J Magn Reson Imaging. 2014; 39: 853–865. doi: 10.1002/jmri.24238 PMID: 24395144
8. Donahue KM, Weisskoff RM, Burstein D. Water diffusion and exchange as they influence contrast enhancement. J Magn Reson Imaging. 1997; 7: 102–110. PMID: 9039599
9. Li X, Rooney WD, Springer CS,Jr. A unified magnetic resonance imaging pharmacokinetic theory: intravascular and extracellular contrast reagents. Magn Reson Med. 2005; 54: 1351–1359. doi: 10.1002/mrm.20684 PMID: 16247739
10. Landis CS, Li X, Telang FW, Coderre JA, Micca PL, Rooney WD, et al. Determination of the MRI contrast agent concentration time course in vivo following bolus injection: effect of equilibrium transcytolemmal water exchange. Magn Reson Med. 2000; 44: 563–574. PMID: 11025512
11. Huang W, Tudorica LA, Li X, Thakur SB, Chen Y, Morris EA, et al. Discrimination of benign and malignant breast lesions by using shutter-speed dynamic contrast-enhanced MR imaging. Radiology. 2011; 261: 394–403. doi: 10.1148/radiol.11102413 PMID: 21828189
12. Springer CS, Jr, Li X, Tudorica LA, Oh KY, Roy N, Chui SY, et al. Intratumor mapping of intracellular water lifetime: metabolic images of breast cancer? NMR Biomed. 2014; 27: 760–773. doi: 10.1002/nbm.3111 PMID: 24798066
13. Tofts PS, Brix G, Buckley DL, Evelhoch JL, Henderson E, Knopp MV, et al. Estimating kinetic parameters from dynamic contrast-enhanced T(1)-weighted MRI of a diffusable tracer: standardized quantities and symbols. J Magn Reson Imaging. 1999; 10: 223–232. PMID: 10508281
14. Yankeelov TE, Rooney WD, Li X, Springer CS Jr. Variation of the relaxographic "shutter-speed" for transcytolemmal water exchange affects the CR bolus-tracking curve shape. Magn Reson Med. 2003; 50: 1151–1169. doi: 10.1002/mrm.10624 PMID: 14648563
15. Sourbron SP, Buckley DL. On the scope and interpretation of the Tofts models for DCE-MRI. Magn Reson Med. 2011; 66: 735–745. doi: 10.1002/mrm.22861 PMID: 21384424
16. Brix G, Bahner ML, Hoffmann U, Horvath A, Schreiber W. Regional blood flow, capillary permeability, and compartmental volumes: measurement with dynamic CT—initial experience. Radiology. 1999; 210: 269–276. PMID: 9885619
17. Brix G, Griebel J, Kiessling F, Wenz F. Tracer kinetic modelling of tumour angiogenesis based on dynamic contrast-enhanced CT and MRI measurements. Eur J Nucl Med Mol Imaging. 2010; 37 Suppl 1: S30–51. doi: 10.1007/s00259-010-1448-7 PMID: 20503049
18. St Lawrence KS, Lee TY. An adiabatic approximation to the tissue homogeneity model for water exchange in the brain: I. Theoretical derivation. J Cereb Blood Flow Metab. 1998; 18: 1365–1377. doi: 10.1097/00004647-199812000-00011 PMID: 9850149
19. Sourbron SP, Buckley DL. Tracer kinetic modelling in MRI: estimating perfusion and capillary permeability. Phys Med Biol. 2012; 57: R1–33. doi: 10.1088/0031-9155/57/2/R1 PMID: 22173205
20. Koh TS. On the a priori identifiability of the two-compartment distributed parameter model from residual tracer data acquired by dynamic contrast-enhanced imaging. IEEE Trans Biomed Eng. 2008; 55: 340–344. doi: 10.1109/TBME.2007.910682 PMID: 18232378

21. Koh TS, Bisdas S, Koh DM, Thng CH. Fundamentals of tracer kinetics for dynamic contrast-enhanced MRI. J Magn Reson Imaging. 2011; 34: 1262–1276. doi: 10.1002/jmri.22795 PMID: 21972053

22. Koh TS, Thng CH, Lee PS, Hartono S, Rumpel H, Goh BC, et al. Hepatic metastases: in vivo assessment of perfusion parameters at dynamic contrast-enhanced MR imaging with dual-input two-compartment tracer kinetics model. Radiology. 2008; 249: 307–320. doi: 10.1148/radiol.2483071958 PMID: 18695207

23. Orton MR, d'Arcy JA, Walker-Samuel S, Hawkes DJ, Atkinson D, Collins DJ, et al. Computationally efficient vascular input function models for quantitative kinetic modelling using DCE-MRI. Phys Med Biol. 2008; 53: 1225–1239. doi: 10.1088/0031-9155/53/5/005 PMID: 18296759

24. Sourbron S, Luypaert R, Morhard D, Seelos K, Reiser M, Peller M. Deconvolution of bolus-tracking data: a comparison of discretization methods. Phys Med Biol. 2007; 52: 6761–6778. doi: 10.1088/0031-9155/52/22/014 PMID: 17975296

25. Koh TS, Cheong DL, Hou Z. Issues of discontinuity in the impulse residue function for deconvolution analysis of dynamic contrast-enhanced MRI data. Magn Reson Med. 2011; 66: 886–892. doi: 10.1002/mrm.22868 PMID: 21465544

26. Moré JJ, Garbow BS, Hillstrom KE. User Guide for MINPACK-1. 1980.

27. Markwardt CB. Non-linear least squares fitting in IDL with MPFIT. In Proc Astronomical Data Analysis Software and Systems XVIII, Quebec, Canada, ASP Conference Series. 2009;411: 251.

28. Molinaro AM, Simon R, Pfeiffer RM. Prediction error estimation: a comparison of resampling methods. Bioinformatics. 2005; 21: 3301–3307. doi: 10.1093/bioinformatics/bti499 PMID: 15905277

29. Simon RM, Subramanian J, Li MC, Menezes S. Using cross-validation to evaluate predictive accuracy of survival risk classifiers based on high-dimensional data. Brief Bioinform. 2011; 12: 203–214. doi: 10.1093/bib/bbr001 PMID: 21324971

30. Simon R, Lam A, Li MC, Ngan M, Menenzes S, Zhao Y. Analysis of gene expression data using BRB-ArrayTools. Cancer Inform. 2007; 3: 11–17. PMID: 19455231

31. Zhao Y, Simon R. BRB-ArrayTools Data Archive for human cancer gene expression: a unique and efficient data sharing resource. Cancer Inform. 2008; 6: 9–15. PMID: 19259398

32. R Core Team. R: A Language and Environment for Statistical Computing: Vienna: R Foundation for Statistical Computing; 2013.

33. Bains LJ, McGrath DM, Naish JH, Cheung S, Watson Y, Taylor MB, et al. Tracer kinetic analysis of dynamic contrast-enhanced MRI and CT bladder cancer data: A preliminary comparison to assess the magnitude of water exchange effects. Magn Reson Med. 2010; 64: 595–603. doi: 10.1002/mrm.22430 PMID: 20665802

34. Paudyal R, Poptani H, Cai K, Zhou R, Glickson JD. Impact of transvascular and cellular-interstitial water exchange on dynamic contrast-enhanced magnetic resonance imaging estimates of blood to tissue transfer constant and blood plasma volume. J Magn Reson Imaging. 2013; 37: 435–444. doi: 10.1002/jmri.23837 PMID: 23197427

35. Zhang J, Kim S. Uncertainty in MR tracer kinetic parameters and water exchange rates estimated from T-weighted dynamic contrast enhanced MRI. Magn Reson Med. 2013. doi: 10.1002/mrm.24927

36. Kim YR, Rebro KJ, Schmainda KM. Water exchange and inflow affect the accuracy of T1-GRE blood volume measurements: implications for the evaluation of tumor angiogenesis. Magn Reson Med. 2002; 47: 1110–1120. doi: 10.1002/mrm.10175 PMID: 12111957

37. Wu XZ, Xie GR, Chen D. Hypoxia and hepatocellular carcinoma: The therapeutic target for hepatocellular carcinoma. J Gastroenterol Hepatol. 2007; 22: 1178–1182. doi: 10.1111/j.1440-1746.2007.04997.x PMID: 17559361

38. Zhu AX, Duda DG, Sahani DV, Jain RK. HCC and angiogenesis: possible targets and future directions. Nat Rev Clin Oncol. 2011; 8: 292–301. doi: 10.1038/nrclinonc.2011.30 PMID: 21386818

39. Hockel M, Vaupel P. Tumor hypoxia: definitions and current clinical, biologic, and molecular aspects. J Natl Cancer Inst. 2001; 93: 266–276. PMID: 11181773

40. Osawa Y, Seki E, Brenner DA. Apoptosis in liver injury and liver diseases. In: Yin X, Dong Z, editors. Essentials of apoptosis: a guide for basic and clinical research. Humana Press; 2009. pp. 556.

41. Haider MA, Milosevic M, Fyles A, Sitartchouk I, Yeung I, Henderson E, et al. Assessment of the tumor microenvironment in cervix cancer using dynamic contrast enhanced CT, interstitial fluid pressure and oxygen measurements. Int J Radiat Oncol Biol Phys. 2005; 62: 1100–1107. doi: 10.1016/j.ijrobp.2004.12.064 PMID: 15990015

42. Wilson WR, Hay MP. Targeting hypoxia in cancer therapy. Nat Rev Cancer. 2011; 11: 393–410. doi: 10.1038/nrc3064 PMID: 21606941

43. Czabanka M, Vinci M, Heppner F, Ullrich A, Vajkoczy P. Effects of sunitinib on tumor hemodynamics and delivery of chemotherapy. Int J Cancer. 2009; 124: 1293–1300. doi: 10.1002/ijc.24019 PMID: 19101989

44. Newsom J, Jones RN, Hofer SM. Longitudinal Data Analysis: A Practical Guide for Researchers in Aging, Health, and Social Sciences: New York: Routledge, Taylor & Francis Group; 2011.

45. Tofts PS. Modeling tracer kinetics in dynamic Gd-DTPA MR imaging. J Magn Reson Imaging. 1997; 7: 91–101. PMID: 9039598

46. Gordon MJ, Chu KC, Margaritis A, Martin AJ, Ethier CR, Rutt BK. Measurement of Gd-DTPA diffusion through PVA hydrogel using a novel magnetic resonance imaging method. Biotechnol Bioeng. 1999; 65: 459–467. doi: 10.1002/(SICI)1097-0290(19991120)65:4<459::AID-BIT10>3.0.CO;2-O [pii]. PMID: 10506421

47. Barsky D, Putz B, Schulten K. Theory of heterogeneous relaxation in compartmentalized tissues. Magn Reson Med. 1997; 37: 666–675. PMID: 9126940

48. Buckley DL, Parker GJM. Measuring Contrast Agent Concentration in T1-Weighted Dynamic Contrast-Enhanced MRI. In: Jackson A, Buckley DL, Parker GJM, editors.: Springer Berlin Heidelberg; 2005. pp. 69–79. doi: 10.1007/3-540-26420-5_5

49. Larsson HB, Rosenbaum S, Fritz-Hansen T. Quantification of the effect of water exchange in dynamic contrast MRI perfusion measurements in the brain and heart. Magn Reson Med. 2001; 46: 272–281. doi: 10.1002/mrm.1188 [pii]. PMID: 11477630

50. Jain R, Gutierrez J, Narang J, Scarpace L, Schultz LR, Lemke N, et al. In vivo correlation of tumor blood volume and permeability with histologic and molecular angiogenic markers in gliomas. AJNR Am J Neuroradiol. 2011; 32: 388–394. doi: 10.3174/ajnr.A2280 PMID: 21071537

51. Larsson HB, Courivaud F, Rostrup E, Hansen AE. Measurement of brain perfusion, blood volume, and blood-brain barrier permeability, using dynamic contrast-enhanced T(1)-weighted MRI at 3 tesla. Magn Reson Med. 2009; 62: 1270–1281. doi: 10.1002/mrm.22136 PMID: 19780145

52. Turetschek K, Preda A, Novikov V, Brasch RC, Weinmann HJ, Wunderbaldinger P, et al. Tumor microvascular changes in antiangiogenic treatment: assessment by magnetic resonance contrast media of different molecular weights. J Magn Reson Imaging. 2004; 20: 138–144. doi: 10.1002/jmri.20049 PMID: 15221819

53. Bhujwalla ZM, Artemov D, Natarajan K, Solaiyappan M, Kollars P, Kristjansen PE. Reduction of vascular and permeable regions in solid tumors detected by macromolecular contrast magnetic resonance imaging after treatment with antiangiogenic agent TNP-470. Clin Cancer Res. 2003; 9: 355–362. PMID: 12538488

54. Li X, Rooney WD, Varallyay CG, Gahramanov S, Muldoon LL, Goodman JA, et al. Dynamic-contrast-enhanced-MRI with extravasating contrast reagent: rat cerebral glioma blood volume determination. J Magn Reson. 2010; 206: 190–199. doi: 10.1016/j.jmr.2010.07.004 PMID: 20674422

55. Landis CS, Li X, Telang FW, Molina PE, Palyka I, Vetek G, et al. Equilibrium transcytolemmal water-exchange kinetics in skeletal muscle in vivo. Magn Reson Med. 1999; 42: 467–478. PMID: 10467291